

Integration of Metal-Organic Frameworks into a 3D Interconnected Network for Improved Ion Transport

Qinghan Zeng

Guangdong University of Technology

Jia Wang

Guangdong University of Technology

Xin Li

Guangdong University of Technology

Yangyuan Ou

Guangdong University of Technology

Wenchao He

Guangdong University of Technology

Dixiong Li

Guangdong University of Technology

Sijia Guo

Guangdong University of Technology

Yingbo Xiao

Guangdong University of Technology

Haoyan Deng

Guangdong University of Technology

Wei Gong

Guangdong University of Technology

Qi Zhang

Guangdong University of Technology

Shaoming Huang (✉ smhuang@gdut.edu.cn)

Guangdong University of Technology

Article

Keywords: metal-organic frameworks (MOFs), batteries, energy storage

Posted Date: January 22nd, 2021

DOI: <https://doi.org/10.21203/rs.3.rs-140199/v1>

License: © ⓘ This work is licensed under a Creative Commons Attribution 4.0 International License.

[Read Full License](#)

Abstract

Metal-organic frameworks (MOFs) have attracted intensive study as solid electrolytes (SEs) in recent years, especially on facilitating ion transport with functionalized channels. However, MOF particles work separately in SEs and numerous interfaces hinder the high-efficiency ion transport, which lowers the performance of solid-state batteries (SSBs) especially at high C-rate. Herein, we constructed continuous ion pathways by integration of MOFs into a 3D interconnected network. Particle arrays of a newly developed MOF (Zr-BPDC-2SO₃H) which has single ion transport ability were grown on the bacterial cellulose (BC) nanofibers to provide a linear ion transport network. The interconnected MOFs network exhibits higher ionic conductivity of $7.88 \times 10^{-4} \text{ S cm}^{-1}$ at 25 °C, single ion transport ability ($t_{\text{Li}^+}=0.88$), wide electrochemical window up to 5.15 V, excellent interface compatibility and capability for suppressing lithium dendrites. Most importantly, the SSB fabricated with the interconnected MOFs network shows more than 100% improved specific capacity than the SSB without integration and stable cycling performance at 3 C. This work demonstrates the effectiveness of integrated design and paves new way for developing high-performance SEs based on porous ion conductors.

Introduction

Lithium metal battery appears to be highly promising for energy storage owing to its high energy density¹⁻³. However, the unsafety of liquid lithium metal battery hinders its applications because of the flammable organic liquid electrolytes and lithium dendrites as well. Additionally, it also suffers from the narrow electrochemical window and the relatively low Li⁺ transference number (usually lower than 0.4)⁴. Solid electrolytes (SEs) are therefore applied to overcome the drawbacks of liquid electrolytes and suppress the growth of lithium dendrites⁵. SEs can be mainly classified into three categories: organic polymeric SEs, inorganic SEs and composite ones. Organic polymeric SEs, such as poly(ethylene oxide) (PEO) and poly(vinylidene fluoride-co-hexafluoropropylene) (PVDF-HFP)^{6,7}, are featured with excellent flexibility and low interfacial resistance. However, their comparatively low ionic conductivities (10^{-6} - $10^{-9} \text{ S cm}^{-1}$) at room temperature restrain their applications, whereas inorganic SEs such as garnet-type Li₅La₃Zr₂O₁₂ (LLZO) and Li₂S-P₂S₅ possess comparable ionic conductivity to that of liquid electrolytes^{8,9}. Unfortunately, the inorganic SEs often induce poor interfacial contact between the electrodes and the SE, and lithium dendrites tend to grow along the grain boundaries^{10,11}. One strategy to overcome the disadvantages of polymeric and inorganic SEs is to use composite of polymeric and inorganic SEs¹². However, the composite still does not satisfy the requirements of SEs in term of ionic conductivity, stability, safety etc. Another strategy, therefore, is to develop new kind of SE with high ion conductivity and ion transference number, wide electrochemical windows, good interfacial contact, and chemical/thermal stability.

Porous materials, such as metal-organic frameworks (MOFs), are expected to address the above-mentioned requirements by virtue of their talents in porosity, physiochemical designability and structure engineering¹³⁻²⁰. For example, the numerous pores in MOFs are capable of storing guest molecules such

as ionic liquids containing Li^+ (Li-IL), which can assist the transport of Li^+ ^{21,22}. Chemical designability affords MOFs with intrinsic ionic conductivity because of the electronegative chemical groups functionalized inside the pores, and the ability for single ion transport. However, how to enhance the intrinsic ionic conductivity and improve the interface between the MOFs particles as well as MOFs and electrodes still remains a big challenge. Although a lot efforts have been devoted to raise the ion conductivity of MOFs intrinsically^{23,24}. For example, CuBTC, HSPE-1-8, P@CMOF and UiOLiTFSI with ion conductive groups have been reported to have ionic conductivity up to $10^{-4} \text{ S cm}^{-1}$ with certain liquid electrolytes²⁵⁻²⁸. It should be also noted that the Li^+ transport is a multidimensional process in MOF-based electrolytes, involving the transport along the conductive channel in MOF particles, between different MOF particles and on the interface of MOFs and electrodes²⁹. In previous reports, the MOF particles function separately and ions transport across the interface of separated particles in sequence, which lowers the specific capacity and cycling performance of the SSBs. Therefore, to construct a transport pathway for Li^+ between MOF particles and reduce the interfacial resistance between MOFs and electrodes, as well as to understand the transport mechanism are of vital importance to realize the use of MOFs as SE in high-performance lithium metal batteries.

Hereby, we propose a novel strategy to fabricate interconnected structure of MOFs to eliminate the interface between MOF particles, as well as build a linear pathway for ion transport as illustrated in Fig. 1. To realize the efficient ion transport within MOF, a MOF functionalized with high-density electronegative groups (Zr-BPDC-2SO₃H) was firstly designed, in which the functional groups can facilitate the ion transport along pore channels as shown in Fig. 1b. More importantly, the nanosized ion conductive MOF particles with interconnected structure were in-situ synthesized on the network of a bacterial cellulose (BC) skeleton (Fig. 1b). Furthermore, a flexible interconnected network of conductive MOF can be obtained by virtue of the network of BC, which will provide integrated three-dimensional pathways for ion transport. Compared with the SE fabricated with conventional mixing strategy (MOFs/PVDF-HFP), the interconnected MOFs network exhibits excellent single ion transport ability ($\lambda_{\text{Li}^+}=0.88$), much lower interfacial resistance (74 Ω), wider electrochemical windows (5.15V) and outstanding effect for suppressing the lithium dendrites. Most importantly, the interconnected MOF-based SE delivers a capacity as high as 119 mA h g⁻¹ at 3 C (more than 100% higher than that of the SSB without integration) and demonstrates a great improvement of cycling performance at high C-rate.

Results

In order to obtain a MOF with excellent Li^+ conductivity, H₂BPDC-2SO₃H (2',5'-disulfo-[1,1':4',1''-terphenyl]-3,3'',5,5''-tetracarboxylic acid), with high-density electronegative groups (-SO₃H) and Zr⁴⁺ ions, were chosen as the ligand and metal nodes to construct a stable MOF framework. The MOF (Zr-BPDC-2SO₃H) with an average particle size of 500 nm was obtained via solvothermal reaction (Supplementary Fig. 1). As shown in Fig. 2a and b, the MOF is isostructural to the reported UiO-67 with a fcu topology.¹⁹ Four weak peaks at 2 θ of 2 to 8 degrees (indicated by arrows) can be observed in the XRD pattern of Zr-

BPDC-2SO₃H (Fig. 2b), which can be ascribed to the existence of correlated defect nano regions in crystals³⁰. The N₂ adsorption isotherm collected at 77 K shows a much smaller Brunauer-Emmett-Teller (BET) surface area of 231.2 m² g⁻¹ compared with that of UiO-67 (2500 m² g⁻¹)³¹, due to the high density -SO₃H groups in pores (Supplementary Fig. 2).

The large amounts of -SO₃H groups are expected to serve as ion hopping sites because of its electronegativity and possible coulomb force toward metal ions, which can then enhance the ability of MOF for ion transport. The ionic conductivities of Zr-BPDC-2SO₃H for various metal ions were thus investigated. Zr-BPDC-2SO₃H powders were treated in PC (propylene carbonate) solutions with different metal ions and pressed under 6 Mpa to obtain pellets of Zr-BPDC-2SO₃M (M = Li⁺, Na⁺, K⁺, Zn²⁺). The electrochemical impedance spectroscopy (EIS) of Zr-BPDC-2SO₃M was collected at a wide range of temperatures (from -20 to 60 °C) (Supplementary Fig. 3). Figure 2c summarizes the EIS of Zr-BPDC-2SO₃M at room temperature and the corresponding ionic conductivities of MOFs for Li⁺, Na⁺, K⁺ and Zn²⁺ are determined to be 2.65 × 10⁻⁴, 1.68 × 10⁻⁴, 5.54 × 10⁻⁵ and 1.9 × 10⁻⁴ S cm⁻¹, respectively. Moreover, the ionic conductivities gradually rise as the increment of temperature, and the activation energy (E_a) for corresponded ions derived from Fig. 2d are calculated to be 0.16, 0.19, 0.27 and 0.21 eV, respectively. To reveal the role of the functional groups in ion transport, the interaction between Li⁺ and MOF was studied by X-ray photoelectron spectra (XPS) with dry Zr-BPDC-2SO₃Li (Supplementary Fig. 4). The characteristic signal of Li-N group in LiTFSI can be observed at 56.2 eV, however, it disappeared in Zr-BPDC-2SO₃Li while a new peak at 54.3 eV emerged, which can be assigned to Li-O bond, indicating the interaction between Li⁺ and -SO₃⁻.

As ionic conductivity is determined by the movement of both positive and negative ions, ion transference number refers to the conductivity contributed solely by the movement of positive ions. In this work, ion transference number of Li⁺ (t_{Li⁺}) was characterized as an example with a composite membrane, Zr-BPDC-2SO₃Li⁺/PVDF-HFP, consisting of 20 wt% of PVDF-HFP (poly(vinylidene-fluoride-co-hexafluoropropylene)) and 80% Zr-BPDC-2SO₃Li⁺. The Zr-BPDC-2SO₃Li⁺/PVDF-HFP membrane exhibits good flexibility and mechanical strength (Supplementary Fig. 5a). t_{Li⁺} was calculated from the current-time curve and the ac impedance spectra before and after polarization using Li|Li symmetric cells referring to the Evans method at room temperature³². As shown in Supplementary Fig. 6, the initial current reached 5.07 μA and then stabilized at 4.01 μA after 3600s. The corresponding t_{Li⁺} of Zr-BPDC-2SO₃H is 0.86, which is excellent compared with other reported porous Li⁺ conductors (Supplementary Table 1 and Supplementary Fig. 7a). Considering the design strategy and the interaction between Li⁺ and -SO₃⁻, it is assumed that the high-density electronegative groups (-SO₃H) in pores offers abundant hopping sites for Li⁺, which can greatly promote the transport of Li⁺ without the movement of electronegative -SO₃⁻ under the electric field.

To apply MOFs as SEs in solid batteries, mixing MOFs with polymers is the most typical way to fabricate a flexible SE membrane^{23,33}. However, in this case, there is hardly chemical contact between MOF particles and thus the ion transport through the interface between MOF particles becomes challenging due to the lack of conductive medium. To solve this problem, in this work, the ion conductive MOF was *in-situ* synthesized on the framework of BC nanofibers and an interconnected MOFs network was obtained. BC was chosen here for its well-arranged linear chain and 3D structure. Both the peaks of Zr-BPDC-2SO₃H and BC nanofiber can be observed in the PXRD pattern of interconnected MOFs network (Supplementary Fig. 8), suggesting that the structure of MOF particles in the network remains the same as the separately synthesized Zr-BPDC-2SO₃H crystals. As shown in Fig. 3a, BC serves as a template, and Zr-BPDC-2SO₃H completely covers the nanofibers of BC in the form of particle arrays without intervals, which is expected to be exempt from the long-distance ion transport and high interfacial resistance between the physically contacted individual particles in the mixture of MOF/polymer. Moreover, nodes can be observed between MOF arrays in the enlarged view, which results in an interconnected 3D network. The mass ratio of MOF and BC nanofiber in the interconnected MOFs network was determined to be 7:3. The cross-sectional view in Fig. 3b shows that the interconnected MOFs network has a uniform thickness of about 86.9 μm. The ion transport ability of the interconnected MOFs network was also investigated. The interconnected MOFs network shows an Li⁺ conductivity of $7.88 \times 10^{-4} \text{ S cm}^{-1}$ with less than 17.63 wt% PC in pores (Supplementary Fig. 9b, d), which is higher than that of the pellet of Zr-BPDC-2SO₃H powders ($2.65 \times 10^{-4} \text{ S cm}^{-1}$, 27.62 wt% PC in pores, Supplementary Fig. 9a, c). Moreover, the ion transference number of the interconnected MOF networks is as high as 0.88, indicating that the network inherits the excellent single ion transport ability of Zr-BPDC-2SO₃H (Fig. 3d) and the transference number is higher than that of previously reported MOFs based SEs (Supplementary Fig. 7a, Supplementary Table 1).

The electrochemical stability of the interconnected MOFs network was investigated by studying the electrochemical window determined by linear sweep voltammetry (LSV) using a stainless steel (ss)|SE|Li cell at room temperature. Zr-BPDC-2SO₃H/BC composite membrane (Supplementary Fig. 5b) with the same composition as interconnected MOFs network (MOF wt%: BC wt% =7:3), BC nanofiber and Zr-BPDC-2SO₃Li⁺/PVDF-HFP were also investigated for comparison. As shown in Fig. 3e, the electrochemical window of interconnected MOFs network is 5.15 V (vs. Li/Li⁺), which is much wider than that of BC nanofiber (4.68 V), Zr-BPDC-2SO₃H/BC (4.91 V) and Zr-BPDC-2SO₃Li⁺/PVDF-HFP (4.4 V). These results obviously indicate that the interconnected MOFs network has wider electrochemical window, which can be attributed to the good electrochemical stability of Zr-BPDC-2SO₃H. The higher electrochemical stability of the interconnected MOFs network will guarantee its stable working as SE in SSB. The EIS Nyquist plots of Li|SE|Li symmetric cells were measured to investigate the interfacial compatibility between electrode and different Zr-BPDC-2SO₃H-based SEs. It can be seen in Fig. 3f that the Li|MOF-based network|Li cell possesses the lowest interface resistance of 74 Ω, smaller than 183 Ω of Li|Zr-BPDC-2SO₃Li⁺/PVDF-HFP|Li cell and 232 Ω of Li|Zr-BPDC-2SO₃H/BC|Li cell. The reason can be ascribed to the different surface morphologies of the SEs (Supplementary Fig. 10). A smooth surface formed by uniform nanosized MOF chains can be observed in the interconnected MOFs network, which is supposed to

benefit the interfacial contact with the electrodes. Whereas, numerous potholes can be observed in Zr-BPDC-2SO₃Li⁺/PVDF-HFP, and aggregation of particles leads to uneven surfaces for Zr-BPDC-2SO₃Li⁺/PVDF-HFP and Zr-BPDC-2SO₃H/BC (Supplementary Fig. 5e, f), resulting in the higher interfacial resistance.

Critical current density (CCD) is determined by the current density at voltage drop during the step increased galvanostatic test and higher CCD represents better capability for suppressing dendrites formation. To evaluate the CCD of different SEs, the current densities of galvanostatic test were step increased and the holding time for one cycle was 1 h using a symmetric Li|SE|Li cell. As shown in Fig. 4a, the voltage increases as the increasing of current density until the short circuit of the cells. Specifically, the Li|MOF-based network|Li shows the lowest voltage at the same current density due to its least interfacial resistance (Fig. 3f). The CCD of the Li|Zr-BPDC-2SO₃Li⁺/PVDF-HFP|Li cell, Li|BC|Li cell and Li|Zr-BPDC-2SO₃H/BC|Li cell are 0.3 mA cm⁻², 0.5 mA cm⁻² and 0.5 mA cm⁻², respectively, while the Li|MOF-based network|Li cell shows an obviously improved CCD of 1.3 mA cm⁻². The Li plating/stripping process during galvanostatic tests were further conducted at RT with Li|SE|Li symmetric cells to study the dendrites suppressing capability of different SEs soaked with PC. As represented in Fig. 4b, the cycling performance of Li-Li symmetric cells fabricated with BC, Zr-BPDC-2SO₃Li⁺/PVDF-HFP and interconnected MOFs network was studied at a fixed current areal capacity of 0.10 mAh cm⁻². For the Li|MOF-based network|Li cell, lowest voltage can be observed and stable lithium plating/stripping can be realized, and no sign of short circuit is observed after 2000 h. By contrast, the Li|BC|Li and Li|Zr-BPDC-2SO₃Li⁺/PVDF-HFP|Li symmetric cell can only work steadily for 200 h and 730 h respectively at a current areal capacity of 0.10 mAh cm⁻², then the polarization voltage becomes unstable and the cell short-circuited. Moreover, Li|MOF-based network|Li symmetric cell can also work for over 2000 h at a current areal capacity of 0.20 mAh cm⁻², as proved in Fig. 4c. All this results certificate that the interconnected MOFs network has remarkably improved capacity for suppressing the growth of lithium dendrites, which matches well with its better interfacial compatibility and electrochemical stability than other compared SEs (Fig. 3e and f).

To interview how the different SEs influence the deposition of Li⁺ on lithium anode, the surface morphologies of lithium plates after 50 cycles of Li plating/stripping at current areal capacity of 0.10 mAh cm⁻² were investigated. Compared with the origin lithium plate (Supplementary Fig. 11a1 and a2), the surface of lithium plate in the Li|interconnected MOFs network|Li symmetric cell is flat and no lithium dendrites are observed (Supplementary Fig. 11d1 and d2). However, lots of protuberance can be observed on the uneven surface of lithium plates in the symmetric cells with BC and Zr-BPDC-2SO₃Li⁺/PVDF-HFP as SEs (Supplementary Fig. 11b1, b2, c1 and c2). The better capability of interconnected MOFs network for optimizing lithium deposition can be ascribed to the smooth and homogeneous surface of interconnected MOFs network. Its homogeneous surface created an even potential energy surface by -SO₃⁻ which can interact with Li⁺ (proved by XPS results in Supplementary Fig. 4) and thus prohibited the inhomogeneous deposition of Li⁺ at interface^{34,35}, resulting in better cycling performance in Li-Li symmetric cells.

Finally, Li metal SSBs were fabricated and the widely used commercial LiFePO_4 , super P and PVDF were mixed as the cathode to investigate the influence of different SEs for battery performance. As shown in Fig. 5a and b, the average discharge capacities of SSB with interconnected MOFs network as SE at 0.2, 0.5, 1, 2, 3 and 5 C are 159, 145, 143, 140, 119 and 108 mA h g^{-1} , respectively. In comparison, the Zr-BPDC- $2\text{SO}_3\text{Li}^+$ /PVDF-HFP and Zr-BPDC- $2\text{SO}_3\text{H}$ /BC based SSBs have similar discharge capacities at low C-rates. However, their discharge capacities decline severely at high C-rates. For instance, the discharge capacity of the SSB with interconnected MOFs network as SE at 3 C is 100% and 200% higher than that of SSBs with Zr-BPDC- $2\text{SO}_3\text{Li}^+$ /PVDF-HFP and Zr-BPDC- $2\text{SO}_3\text{H}$ /BC as SEs. The cycling performance of the SSB fabricated with interconnected MOFs network at 1 C is exhibited in Fig. 5c and d, which retains a stable discharge specific capacity of around 140 mA h g^{-1} after 500 cycles without decay. The cycling performances of SSBs with different SEs at 3 C are compared in Fig. 5e. The SSB fabricated with interconnected MOFs network remains a specific capacity of 119 mA h g^{-1} at 3 C after 600 cycles with a decay rate of 0.02% per cycle (Fig. 5f). However, the SSBs fabricated with BPDC- $2\text{SO}_3\text{Li}^+$ /PVDF-HFP and Zr-BPDC- $2\text{SO}_3\text{H}$ /BC show low and fast decayed specific capacity, indicating their disability for running at high C-rate. Moreover, the unchanged PXRD of interconnected MOFs network after cycling at 3 C proves its electrochemical stability during cycling (Supplementary Fig. 8). Compared with the reported SSBs based on MOFs, the SSB fabricated with interconnected MOFs network shows excellent rate performance and cycling performance especially at high C-rate over 1 C (Supplementary Fig. 7b, Supplementary Table 2). The much better performance of interconnected MOFs network can be ascribed to its integrated linear channels for ion transport, optimized interfacial compatibility and ability for suppressing lithium dendrites certificated by above-mentioned experiments.

Discussion

In summary, it has been proved that a 3D interconnected ion conductive network, which is constructed by newly developed particle arrays of single-ion conductive MOF (Zr-BPDC- $2\text{SO}_3\text{H}$) grown on BC nanofibers, can effectively facilitate the ion transport, leading to improved performance of SSB. The abundant $-\text{SO}_3\text{H}$ groups in pores of the designed MOF, the interconnected architecture of the MOFs arrays and the continuous 3D network together provide a high Li^+ conductivity of $7.88 \times 10^{-4} \text{ S cm}^{-1}$ at 25 °C and an outstanding single-ion transport ability ($t_{\text{Li}^+}=0.88$), wide electrochemical windows (5.15 V), optimized interfacial compatibility and outstanding ability for suppressing lithium dendrites. The SSB fabricated with interconnected MOFs network as SE improves the specific capacity by more than 100% than that of the SSB fabricated with traditional MOF-based SE (MOF/PVDF) and makes the stable long-time cycling at 3 C possible. This outstanding performance of the SSB based on interconnected MOFs network clearly indicates the effectiveness of designing 3D interconnected MOFs network with linear ion transport pathways. The strategy developed in this work could be broadly applicable to other porous SEs and paves the way for developing new-type ion conductors for SSBs.

Methods

Synthesis of Zr-BPDC-2SO₃H

A mixture of H₂BPDC-2SO₃H (161.25 mg, 0.43 mmol) and ZrCl₄ (99.82 mg, 0.43 mmol) was dissolved in a solution of DMF (12 mL) and acetic acid (600 μL). The solution was then added into a 20 mL Teflon-lined autoclave and subjected to ultrasonic treatment for 5 min. Subsequently, the autoclave was kept at 120 °C for 48 h. The sediment was collected by centrifuging and washed with ethanol for 3 times and dried at 60 °C for 12 h.

Synthesis of Zr-BPDC-2SO₃M

Zr-BPDC-2SO₃H was placed in a prepared solution of 1 M LiTFSI, 1 M NaTFSI, 1 M KPF₆ solution and 1 M Zn(ClO₄)₂·6H₂O in PC, respectively. The mixture was then kept in a shaker for 6 hours to adsorb metal cations. Then the solids were obtained by centrifugation and washed with PC and dried at 100 °C. The obtained MOFs are named as Zr-BPDC-2SO₃M (M = Li⁺, Na⁺, K⁺, Zn²⁺). For the XPS test, acetonitrile was used as the solvent and the final sample was dried at 150 °C under vacuum for 12 h.

Synthesis of Zr-BPDC-2SO₃Li⁺/PVDF-HFP

Zr-BPDC-2SO₃Li (400 mg), PVDF-HFP (100 mg) and LiTFSI (57 mg) were mixed in DMF. After magnetically stirring for 24 h, the mixture was casted onto cleaned petri dishes and prebaked for half an hour under infrared lamp. Then the mixture was further dried at 60 °C under vacuum for 12 h to remove the DMF solvent. The obtained flexible membranes were stored in an argon filled glove box (≤ 0.1 ppm H₂O and O₂) (MIKROUNA).

Synthesis of Zr-BPDC-2SO₃H/BC

70 mg of Zr-BPDC-2SO₃H was dispersed in 5.45 g BC suspension (0.55 wt%) with 10 mL ethanol added. The mixture was stirred vigorously for 5 h. Finally, the products were collected by vacuum filtration and washed with ethanol several times. The free-standing Zr-BPDC-2SO₃H/BC thus formed after drying at 60 °C under vacuum for 12 h, which can be easily peeled off the filter membrane. The obtained flexible membranes were cut into circles with a diameter of 16 mm and stored in an argon filled glove box (≤ 0.1 ppm H₂O and O₂) (MIKROUNA).

Synthesis of interconnected MOFs network

The BC nanofibers can be obtained by freeze-drying BC hydrogel for 48 h and be cut into circles with a diameter of 16 mm. Then the BC nanofibers were immersed in ZrCl₄/DMF solution under ultrasonic treatment at room temperature for about 20 min. The corresponding organic ligands and acetic acid were then added. After dispersing under ultrasonic treatment for 5 min, the mixture was transferred to Teflon-lined autoclave and heated at 120 °C for 48 h. The yielded membranes were washed by ethanol for

several times and dried at 60 °C to obtain white interconnected MOFs network membranes. The obtained membranes were stored in an argon filled glove box (≤ 0.1 ppm H₂O and O₂) (MIKROUNA).

Synthesis of cathode: Commercial LiFePO₄, super-P carbon black and polyvinylidene difluoride (PVDF) were mixed in N-methyl pyrrolidone (NMP) at a mass ratio of 8:1:1 to obtain the cathode mixture. And then the cathode mixture was subsequently coated on aluminium foil. The prepared electrode films were dried at 60 °C for 24 h under vacuum before cell fabrication. The aluminium foil was punched into circles with a diameter of 12 mm. The loading of the active material is around 1.5-2 mg cm⁻².

Declarations

Competing interests

The authors declare no competing interests.

Author contributions

Q.H.Z. and J.W. contributed equally to this work. Q.Z. and S.M.H. proposed the concept and supervised the work. Q.H.Z. synthesized the materials and performed the experiments with the help from J.W., X.L., W.C.H., D.X.L., S.J.G., Y. O., W.G. H.Y.D. and Y.B.X. Q.H.Z., J.W., Q. Z. and S.M.H. analyzed the data and co-wrote the manuscript. All authors discussed the results and commented on the manuscript.

Acknowledgements

The authors gratefully acknowledge financial support from the National Natural Science Foundation of China (No. 51920105004 and 51902060), the Foundation for Young Talents in Higher Education of Guangdong, China (No. 2018KQNCX065) and National Natural Science Foundation of Guangdong, China (No. 2019A1515010842).

Data availability

The data supporting the findings of this study are available within the article and its Supplementary information files. All data is available from the authors upon reasonable request.

References

1. Zeng, X. *et al.* Commercialization of lithium battery technologies for electric vehicles. *Adv. Energy Mater.* **9**, 1900161 (2019).
2. Tan, H., Yu, X. Z., Huang, K., Zhong, J. & Lu, B. Large-scale carambola-like V₂O₅ nanoflowers arrays on microporous reed carbon as improved electrochemical performances lithium-ion batteries cathode. *J. Energy Chem.* **51**, 388-395 (2020).

3. Xia, S., Wu, X., Zhang, Z., Cui, Y. & Liu, W. Practical challenges and future perspectives of all-solid-state lithium-metal batteries. *Chem* **5**, 753-785 (2019).
4. Chen, X. *et al.* A diffusion-reaction competition mechanism to tailor lithium deposition for lithium-metal batteries. *Angew. Chem. Int. Ed.* **59**, 7743-7747 (2020).
5. Zhao, C. Z. *et al.* Liquid phase therapy to solid electrolyte–electrode interface in solid-state Li metal batteries: a review. *Energy Storage Mater.* **24**, 75-84 (2020).
6. Wu, J. *et al.* Ultrathin, flexible polymer electrolyte for cost-effective fabrication of all-solid-state lithium metal batteries. *Adv. Energy Mater.* **9**, 1902767 (2019).
7. Lei, D. *et al.* Cross-linked beta alumina nanowires with compact gel polymer electrolyte coating for ultra-stable sodium metal battery. *Nat. Energy* **10**, 4244 (2019).
8. Duan, H. *et al.* Building an air stable and lithium deposition regulable garnet interface from moderate-temperature conversion chemistry. *Angew. Chem. Int. Ed.* **59**, 12069-12075 (2020).
9. Chen, S. *et al.* Sulfide solid electrolytes for all-solid-state lithium batteries: structure, conductivity, stability and application. *Energy Storage Mater.* **14**, 58-74 (2018).
10. Gao, Z. *et al.* Promises, challenges, and recent progress of inorganic solid-state electrolytes for all-solid-state lithium batteries. *Adv. Mater.* **30**, 1705702 (2018).
11. Xu, L. *et al.* Interfaces in solid-state lithium batteries. *Joule* **2**, 1991-2015 (2018).
12. Zheng, Y. *et al.* A review of composite solid-state electrolytes for lithium batteries: fundamentals, key materials and advanced structures. *Chem. Soc. Rev.* **49**, 8790-8839 (2020).
13. Jiao, L., Seow, J. Y. R., Skinner, W. S., Wang, Z. U. & Jiang, H. L. Metal–organic frameworks: structures and functional applications. *Mater. Today* **27**, 43-68 (2019).
14. Yi, F. *et al.* Metal-organic frameworks and their composites: synthesis and electrochemical applications. *Small Methods* **1**, 1700187 (2017).
15. Cai, X. *et al.* Nano-sized metal-organic frameworks: synthesis and applications. *Coord. Chem. Rev.* **417**, 213366 (2020).
16. Wang, B. *et al.* Cr₂O₃@TiO₂ yolk/shell octahedrons derived from a metal–organic framework for high-performance lithium-ion batteries. *Microporous Mesoporous Mater.* **203**, 86-90 (2015).
17. Ye, Y., Gong, L., Xiang, S., Zhang, Z. & Chen, B. Metal-organic frameworks as a versatile platform for proton conductors. *Adv. Mater.* **32**, 1907090 (2020).
18. Zhang, Q. *et al.* Multivariable sieving and hierarchical recognition for organic toxics in nonhomogeneous channel of MOFs. *Chem* **5**, 1337-1350 (2019).
19. Hobday, C. L. *et al.* A computational and experimental approach linking disorder, high-pressure behavior, and mechanical properties in UiO frameworks. *Angew. Chem. Int. Ed.* **55**, 2401-2405 (2016).
20. Serre, C. Batteries: sieving the ions. *Nat. Energy* **1**, 16100 (2016).
21. Fujie, K., Ikeda, R., Otsubo, K., Yamada, T. & Kitagawa, H. Lithium ion diffusion in a metal–organic framework mediated by an ionic liquid. *Chem. Mater.* **27**, 7355-7361 (2015).

22. Xia, Y. *et al.* Rational design of ion transport paths at the interface of metal–organic framework modified solid electrolyte. *ACS Appl. Mater. Interfaces* **12**, 22930-22938 (2020).
23. Zhang, Q. *et al.* Multiscale optimization of Li-ion diffusion in solid lithium metal battery via ion conductive metal-organic frameworks. *Nanoscale* **12**, 6976-6982 (2020).
24. Li, D. *et al.* Molecular-scale interface engineering of metal–organic frameworks toward ion transport enables high-performance solid lithium metal battery. *Adv. Funct. Mater.* **30**, 2003945 (2020).
25. Shen, L. *et al.* Creating lithium-ion electrolytes with biomimetic ionic channels in metal-organic frameworks. *Adv. Mater.* **30**, 1707476 (2018).
26. Wang, Z. *et al.* Covalently linked metal–organic framework (MOF)-polymer all-solid-state electrolyte membranes for room temperature high performance lithium batteries. *J. Mater. Chem. A* **6**, 17227-17234 (2018).
27. Huo, H. *et al.* Anion-immobilized polymer electrolyte achieved by cationic metal-organic framework filler for dendrite-free solid-state batteries. *Energy Storage Mater.* **18**, 59-67 (2019).
28. Zhu, F. *et al.* High-performance metal-organic framework-based single ion conducting solid-state electrolytes for low-temperature lithium metal batteries. *ACS Appl. Mater. Interfaces* **11**, 43206-43213 (2019).
29. Famprakis, T., Canepa, P., Dawson, J. A., Islam, M. S. & Masquelier, C. J. N. M. Fundamentals of inorganic solid-state electrolytes for batteries. *Nat. Mater* **18**, 1 (2019).
30. Liu, L. *et al.* Imaging defects and their evolution in a metal–organic framework at sub-unit-cell resolution. *Nat. Chem.* **11**, 622-628 (2019).
31. Nickerl, G. *et al.* Integration of accessible secondary metal sites into MOFs for H₂S removal. *Inorg. Chem. Front.* **1**, 325-330 (2014).
32. Evans, J. W., Vincent, C. A. & Bruce, P. G. Electrochemical measurement of transference numbers in polymer electrolytes. *Polymer* **28**, 2324-2328 (1987).
33. Zhang, Q. *et al.* The optimized interfacial compatibility of metal–organic frameworks enables a high-performance quasi-solid metal battery. *ACS Energy Lett.* **5**, 2919-2926 (2020).
34. Shen, K. *et al.* Magnetic field–suppressed lithium dendrite growth for stable lithium-metal batteries. *Adv. Energy Mater.* **9**, 1900260 (2019).
35. Tao, R. *et al.* Kinetics tuning the electrochemistry of lithium dendrites formation in lithium batteries through electrolytes. *ACS Appl. Mater. Interfaces* **9**, 7003-7008 (2017).

Figures

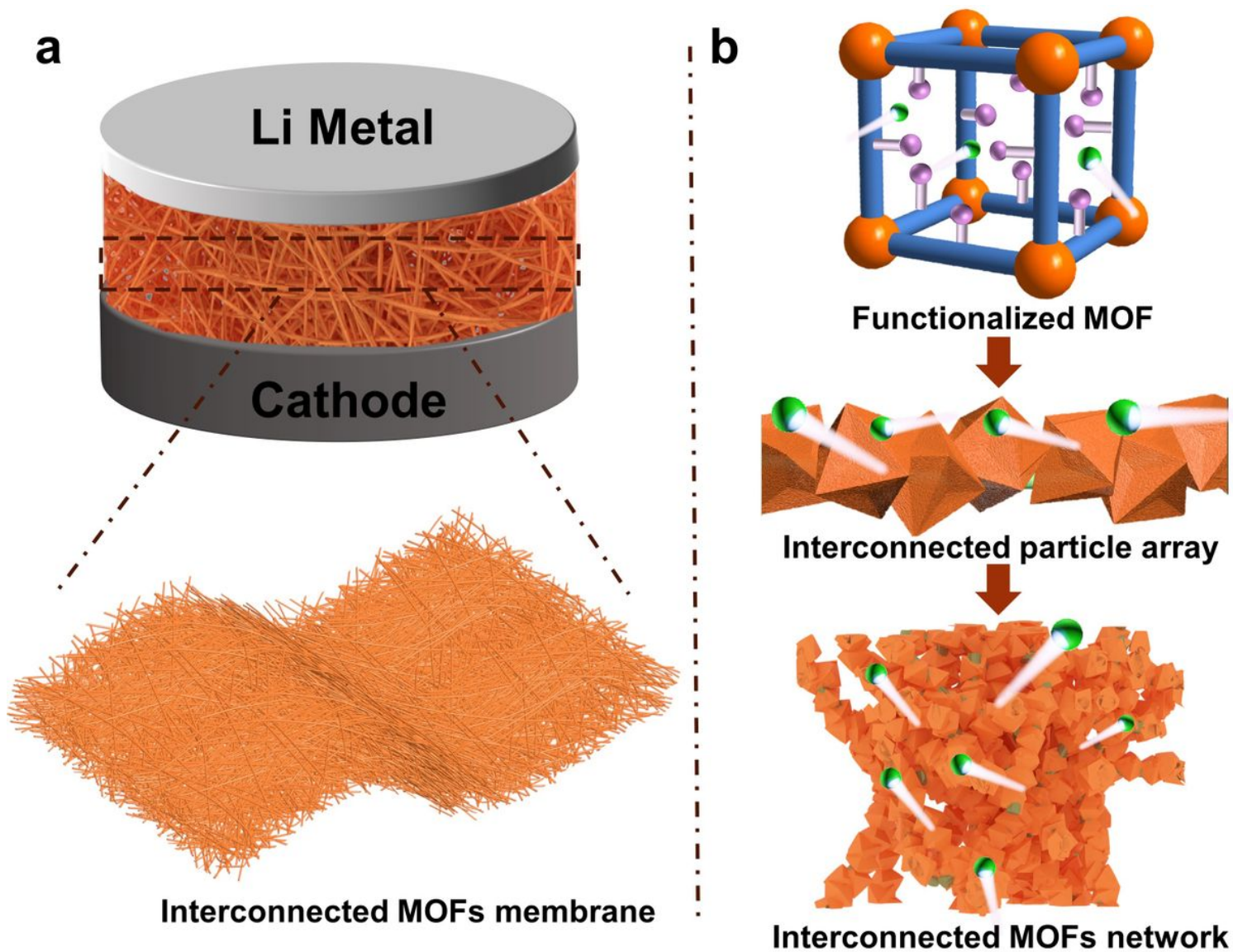


Figure 1

Illustration of the interconnected MOFs network as SE. a The structure of SSB with flexible interconnected MOFs network as SE. b Bottom-up synthesis of interconnected MOFs network on BC skeleton.

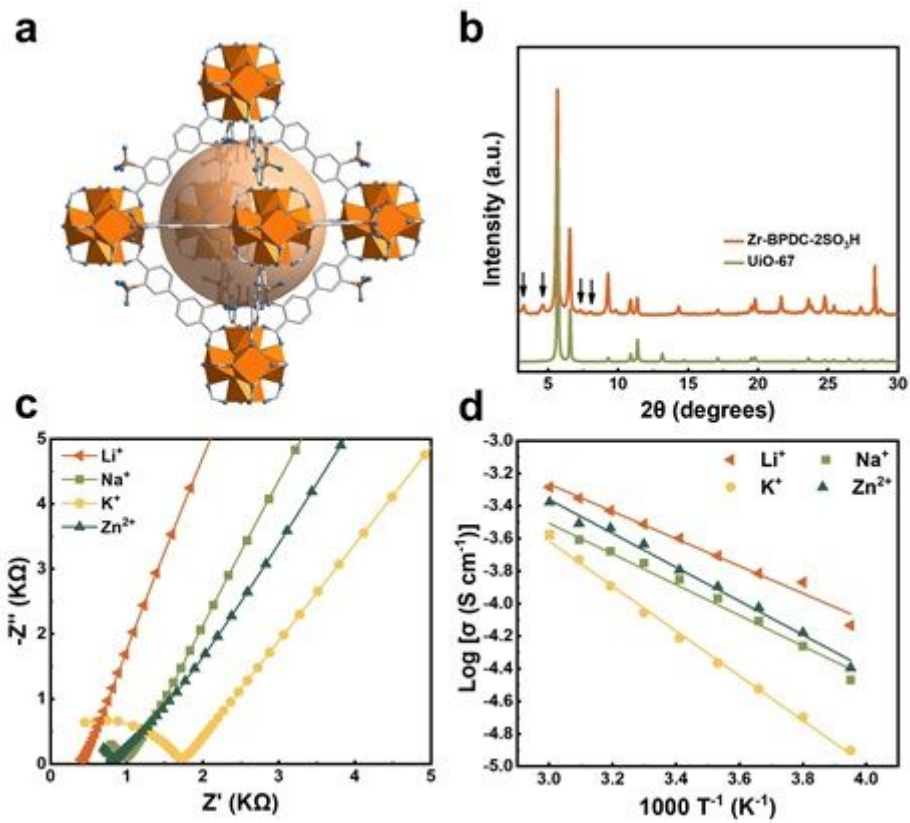


Figure 2

Structural illustration and ionic conductivities of Zr-BPDC-2SO₃H. a Crystal structure of Zr-BPDC-2SO₃H. Color code: Zr, orange; O, blue; C, grey; S, yellow. b PXRD of Zr-BPDC-2SO₃H and UiO-67. c EIS plots of Zr-BPDC-2SO₃H for Li⁺, Na⁺, K⁺, Zn²⁺ at room temperature. d Corresponding Arrhenius plots of the ionic conductivities of Zr-BPDC-2SO₃H for Li⁺, Na⁺, K⁺, Zn²⁺.

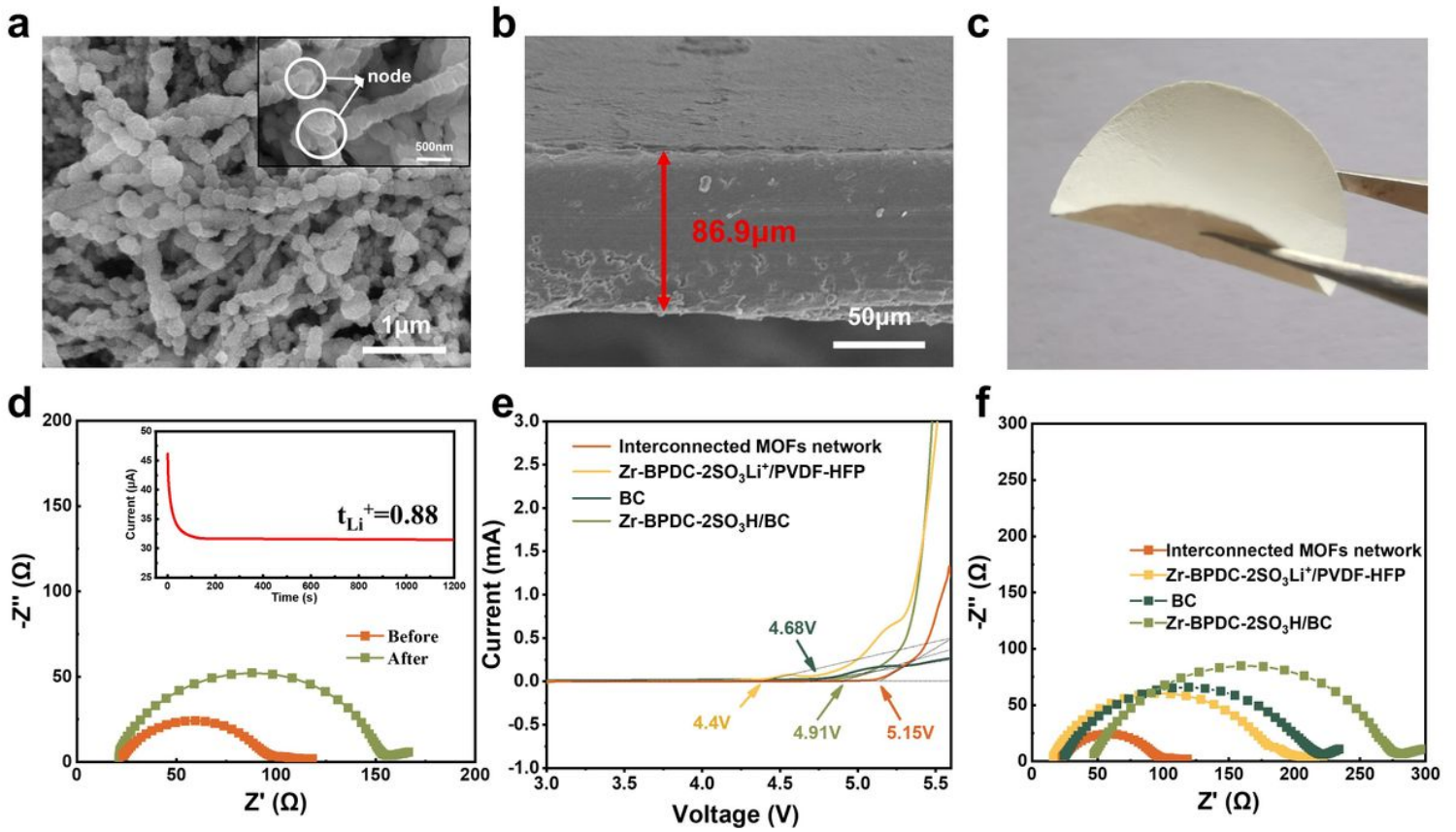


Figure 3

Characterization of the interconnected MOFs network. a, b Top and side views of the interconnected MOFs network membrane, respectively. c Photograph of the interconnected MOFs network membrane. d EIS before and after polarization of the Li|interconnected MOFs network|Li cell, and the inset is the current-time curve at 10 mV of polarization. e LSV profiles of Li|SEs|SS asymmetric cell. f EIS plots of Li|SEs|Li cell.

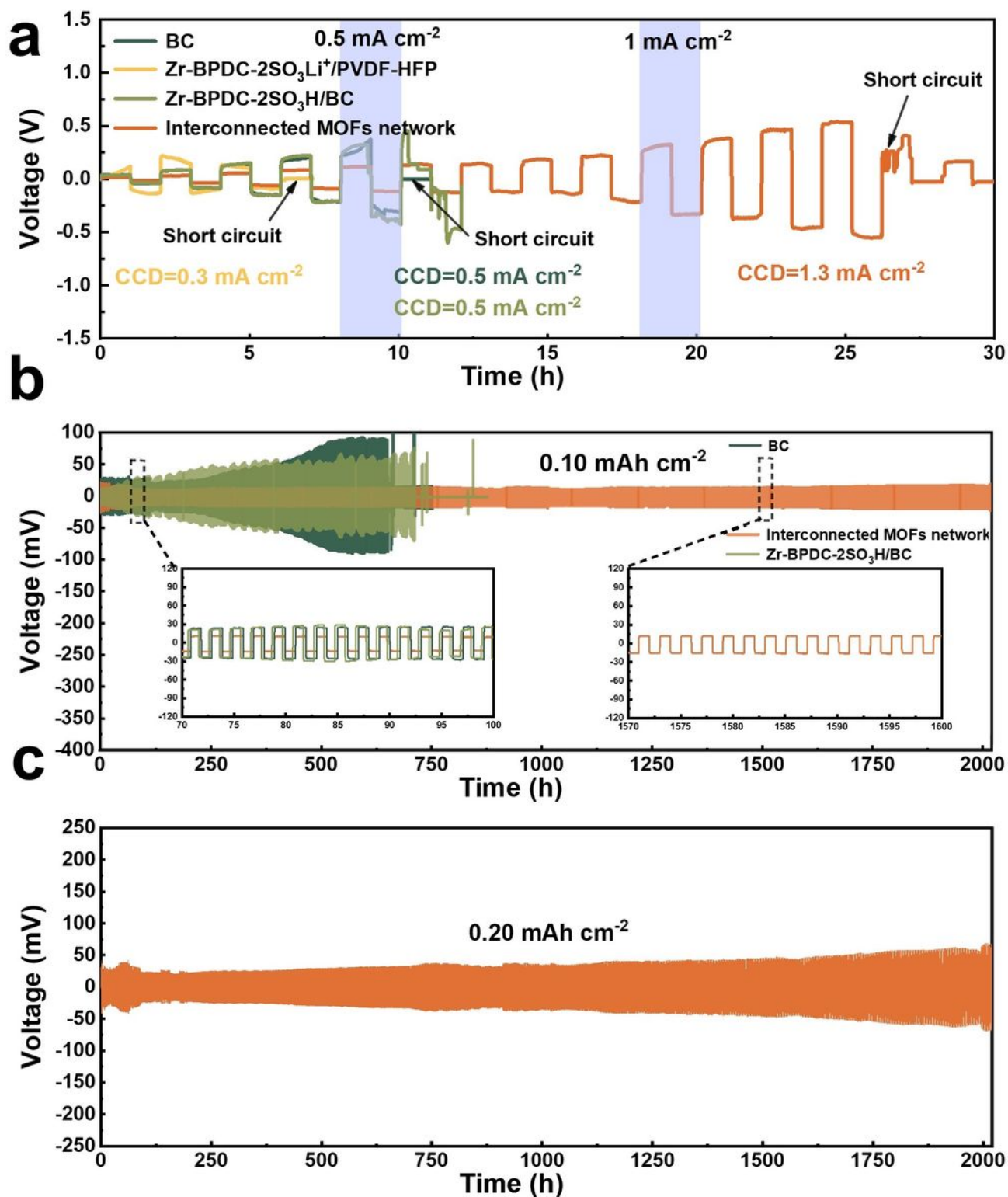


Figure 4

Capabilities of various SEs for suppressing dendrites growth. a CCD of the symmetric Li/Li cell with interconnected MOFs network, BC, Zr-BPDC-2SO₃H/BC and Zr-BPDC-2SO₃Li⁺/PVDF-HFP. b Galvanostatic cycling performance of the symmetric Li/Li cell with interconnected MOFs network, BC and Zr-BPDC-2SO₃H/BC under a current areal capacity of 0.10 mAh cm⁻². c Galvanostatic cycling performance of the symmetric Li/Li cell with interconnected MOFs network under a current areal capacity of 0.20 mAh cm⁻².

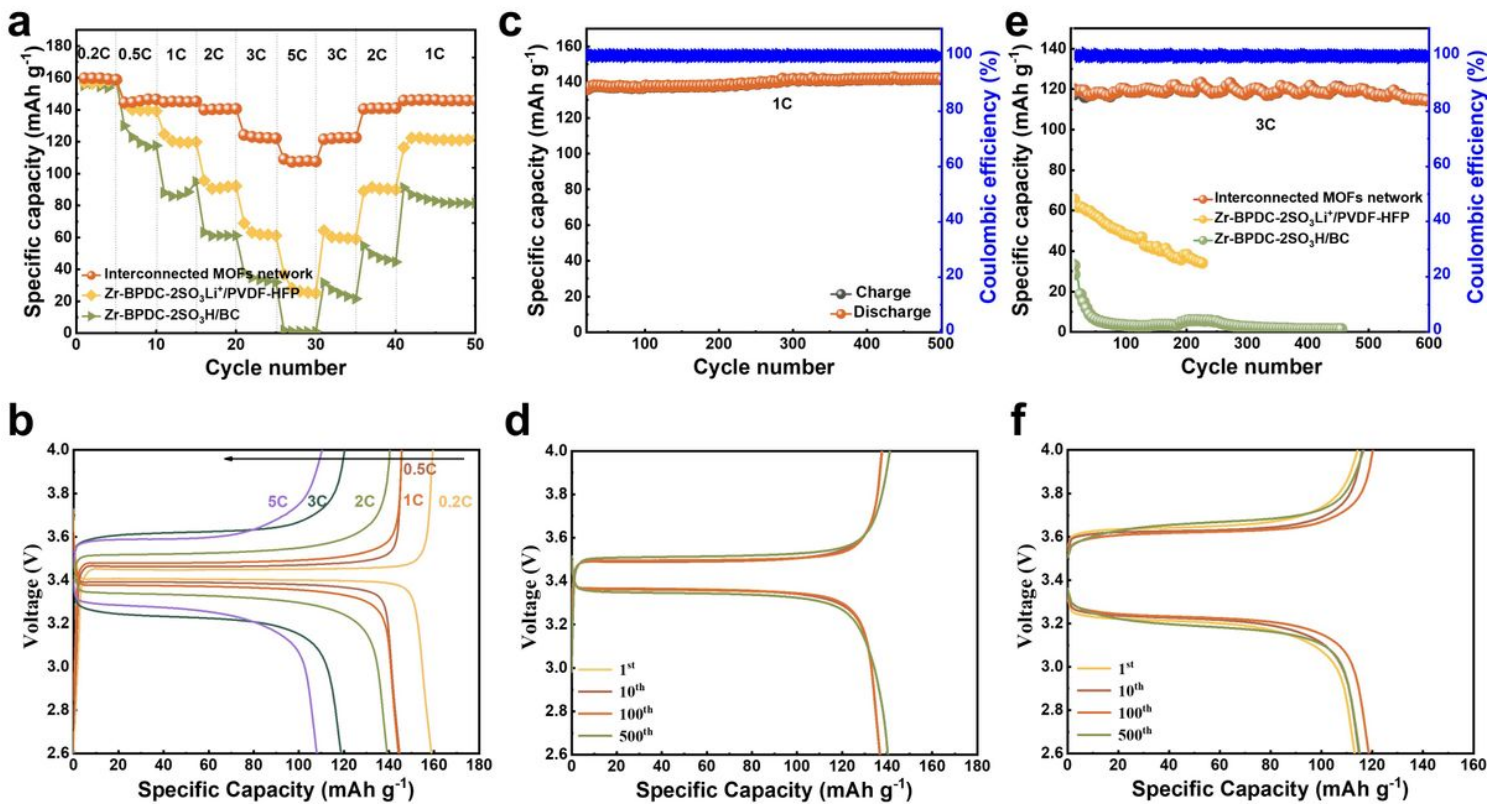


Figure 5

Performance of Li/LFP SSBs with various SEs under room temperature. a C rate performance of SSBs. b Charge-discharge voltage profiles of SSB with interconnected MOFs network. c, d Cycling performance and charge-discharge voltage profiles of SSBs with interconnected MOFs network at 1 C. e Cycling performance of SSBs at 3 C. f Charge-discharge voltage profiles of SSB with interconnected MOFs network at 3 C.

Supplementary Files

This is a list of supplementary files associated with this preprint. Click to download.

- [EXXXXXXXXXXXXXXXXXXXXXXXXXXXXXpaperNCSI.docx](#)